Numerical investigation of the coupled flutter onset mechanism for streamlined bridge deck cross-sections

GIOVANNI CANNATA LUCA BARSI FRANCESCO GALLERANO
Department of Civil, Construction and Environmental Engineering
Sapienza University of Rome
Via Eudossiana 18 - 00184, Roma
ITALY
giovanni.cannata@uniroma1.it

Abstract: - In this work the aeroelastic stability of long-span bridge decks is numerically investigated. A simulation model is presented by which the aerodynamic fields and the structural motion are simultaneously and jointly simulated. The bridge deck is schematised as a bidimensional rigid body subject to elastic restraints corresponding to the torsional and the vertical degree of freedom, and the ALE formulated 2D URANS equations are numerically integrated by a finite volume technique on meshes which deform according to the motion of the structure. The validation of the numerical model is performed by comparing the numerical results with those of an experimental campaign, and is used to investigate the aeroelastic stability of the Forth Road Bridge deck. A profound insight into the onset and the amplification mechanisms of coupled flutter for long-span bridge decks is proposed.

Key-Words: - Bridge aeroelasticity; finite volume; moving grids, turbulence modelling.

1 Introduction

Flutter is an oscillatory aero-elastic phenomenon to which long-span bridge decks are prone. Once the instability is triggered, the amplitudes of oscillation increase fast and the bridge deck is rapidly driven to collapse [1]. Torsional flutter can affect bridge decks with bluff cross-section, as it has been seen in the case of the Tacoma Narrows Bridge deck, and its physical mechanism has been widely investigated by many research groups. It has been recognized that the key to the torsion instability mechanism is the formation and drift of large-scale vortices on the cross-section of the deck [2, 3]. Coupled (torsional-flexural) flutter can involve bridge deck with streamlined cross-section. The risk of coupled flutter is significant if the torsional natural frequency is only slightly larger than the vertical natural frequency, which is usually the case of long-span bridge decks [4]. Bridge deck coupled flutter has been experimentally investigated by Matsumoto et al. [5]. The latter authors distinguish a torsional-branch (TB) coupled flutter and a heaving-branch (HB) coupled flutter. TB coupled flutter looks like a fundamentally torsional motion, with the rotational axis at a certain point apart from mid-chord point. HB coupled flutter looks like a mainly heaving motion with large amplitude, accompanied by a torsional motion with small amplitude.

The identification of the critical flutter wind velocity of bridge decks is usually performed by means of the Scanlan method [6]. In this method, which rests on the assumption of sinusoidal oscillations, the forces produced by the aerodynamic fields on the deck are modelled as linear functions of the structural displacements. This is accomplished by using a set of parameters, named *flutter derivatives*, which can be either estimated numerically and experimentally. As underlined by Astiz [7] and Dowell [1], the linear relationship between the aerodynamic forces and the structural displacements turns out to be adequate only if the deck oscillations have small amplitudes. The same authors stress that this linear relationship does not permit to consider the effects of the unsteady vortices generated by the wind-structure interaction.

By contrast, many authors [8, 9, 4, 10] identify the critical flutter wind velocity by the free motion procedure. In this procedure, the aerodynamic fields and the structural motion are simultaneously and jointly simulated, so that the aeroelastic stability is verified for various wind speeds directly. According to this procedure, the pressure and velocity fluid fields that develop around the structure at every instant are simulated; starting from the aerodynamic pressures, the lift force and the twisting moment acting on the structure at every instant are computed; once the above-mentioned aerodynamic forces are known, the structural displacements are calculated; these displacements, in turn, modify the computational domain and the boundary for

numerical integration of the fluid motion equations and, as a consequence, modify the structure of the aerodynamic fields. With respect to the Scanlan method, the free motion procedure provides more useful insights into the physical mechanisms of the aeroelastic instability.

Finite volume techniques are used by many authors in order to simulate the aerodynamic fields on unstructured grids [11, 12, 13] or on structured grids [14, 15, 16, 17, 18]. Many authors [19, 20, 21] underline that, when the aerodynamic fields are simulated around moving objects, the Arbitrary Lagrangian Eulerian (ALE) formulation has to be applied to the fluid motion equations.

The instabilities of the decks are related to the unsteady phenomena of the aerodynamic fields [2, 22, 23], and in particular to the formation of unsteady vortex structures. The URANS approach makes it possible to simulate the quasi-periodic unsteady vortex structures of the aerodynamic field [24] and (with reference to aeroelastic instability phenomena such as vortex induced vibrations and flutter) to well identify the onset velocities and the amplitudes of the induced structural oscillations [25].

In this work the aeroelastic stability of long-span bridge decks is numerically investigated. A simulation model is presented by which the aerodynamic fields and the structural motion are simultaneously and jointly simulated. The bridge deck is schematised as a bidimensional rigid body subject to elastic restraints corresponding to the torsional and the vertical degree of freedom, and the ALE formulated 2D URANS equations are numerically integrated by a finite volume technique on meshes which deform according to the motion of the structure. The finite volume technique is based on high order weighted essentially non-oscillatory (WENO) reconstructions, and the advancing in time of the solution is carried out through a five stage fourth order accurate strong stability preserving Runge-Kutta (SSPRK) method. By the proposed numerical method it is possible to ensure high accuracy both in space and time. The URANS equations are completed by the turbulent closure relations which are expressed as a function of the turbulent kinetic energy, the turbulence frequency and the strain tensor according to the *k-ω* SST approach. The proposed model is applied to the case study of the Forth Road Bridge deck, and is validated by comparing the obtained numerical results with those of an experimental campaign [15]: in order to perform the above validation, the critical flutter wind velocity and the root mean square of rotational displacements are taken as benchmark parameters. A profound insight into the onset and the amplification mechanisms of coupled flutter for long-span bridge decks is proposed.

2 The proposed model

2.1 The fluid motion equations

The simulation of the aerodynamic field is performed by numerically integrating the ensemble averaged continuity and momentum equations. In integral form, the ALE (Arbitrary Lagrangian-Eulerian) formulated 2D URANS (Unsteady Reynolds-Averaged Navier-Stokes) equations are expressed as follows [26]

$$\frac{d}{dt}\int_{\Delta A} dA + \int_{L} \left[\langle u_i\rangle - u_{g,i}\right] n_i \, dL = 0 \tag{1}$$

$$\begin{aligned}\frac{d}{dt}\int_{\Delta A} \langle u_i\rangle \, dA = &-\int_{L} \langle u_i\rangle \left[\langle u_j\rangle - u_{g,j}\right] n_j \, dL \\ &+ \int_{\Delta A} \frac{\partial}{\partial x_j}\left[2\nu\langle S_{ij}\rangle - \langle u_i' u_j'\rangle\right] dA \\ &+ \int_{\Delta A} f_i \, dA - \int_{\Delta A} \frac{\partial \langle P\rangle}{\partial x_i} \, dA\end{aligned} \tag{2}$$

being $\langle u_i \rangle$ and $\langle P \rangle$ respectively the ensemble-averaged *i-th* fluid velocity component and the ensemble-averaged fluid pressure, $u_{g,i}$ the *i-th* grid velocity component, ν the kinematic fluid viscosity, f_i the *i-th* component of the mass force vector, dA the surface area of an element delimited by the contour line L, and n_j the normal pointing outward. The additional unknown $\langle u_i' u_j' \rangle$, which can be defined as the Reynolds tensor, is modelled based on the Boussinesq assumption

$$\langle u_i' u_j' \rangle = -2\nu_t \langle S_{ij}\rangle + \frac{2}{3}\langle k\rangle \delta_{ij} \tag{3}$$

being $\langle S_{ij} \rangle$ the ensemble averaged strain rate tensor, $\langle k \rangle$ the ensemble averaged turbulent kinetic energy per unit mass, ν_t the kinematic eddy viscosity, δ_{ij} the Kronecker symbol. The turbulent closure relations adopted in this work, together with the calibration parameters herein included, are taken from Menter [27].

2.2 The structural motion equations

By neglecting the displacements in the horizontal direction *x*, the 2D motion of the body can be described in terms of two displacement components, η, θ, where η is the translational displacement of the gravity centre in the vertical direction *y*, and θ is the torsional displacement of the body (rotation). The governing equations for the body motion are expressed as follows

$$m\,\ddot{\eta} + S\,\ddot{\theta} + c_\eta\,\dot{\eta} + k_y\,\eta = f_y(\eta,\dot{\eta},\ddot{\eta},\theta,\dot{\theta},\ddot{\theta}) \quad (4)$$

$$I\,\ddot{\theta} + S\,\ddot{\eta} + c_\theta\,\dot{\theta} + k_\theta\,\theta = m_\theta\,(\eta,\dot{\eta},\ddot{\eta},\theta,\dot{\theta},\ddot{\theta}) \quad (5)$$

being f_y and m_θ the vertical component of the aerodynamic force and the twisting moment generated by the same force, *m* and *I* the structural mass and the structural moment of inertia per unit length, *S* the static imbalance (which is equal to *m* times the distance *a* between the shear centre and the centre of mass), c_y and c_θ the structural damping constants in the vertical and torsional degree of freedom, and k_y and k_θ the stiffness constants of the vertical and the torsional elastic spring. The integration of the pressures, the viscous stresses and the turbulent stresses over the surface of the structure allows the calculation of the force component f_y and the twisting moment m_θ. The stiffness constants are ascribed to give the correct natural frequencies in the fundamental flexural and torsional modes of vibration of the structure. The damping coefficients are derived from the known damping ratios by means of the classical viscous damping assumption. The structural motion equations are solved by a second-order accurate scheme, and the coupling between the fluid solver and the structure solver follows a partitioned loose-coupling approach [28].

2.3 The numerical scheme

In this section we present the finite volume method used for the numerical integration of the fluid motion equations.

Let us define $\langle\overline{u}_i\rangle$ and $\langle\overline{P}\rangle$ as the cell averaged values of the velocity vector and the pressure

$$\langle\bar{u}_i\rangle = \frac{1}{\Delta A}\int_{\Delta A}\langle u_i\rangle\,dA, \quad \langle\bar{P}\rangle = \frac{1}{\Delta A}\int_{\Delta A}\langle P\rangle\,dA \quad (6).$$

The state of the system is known at the centre of the calculation cell and it is defined by the cell-averaged values $\langle\overline{u}_i\rangle$ and $\langle\overline{P}\rangle$. The time level at which the variables are known is *n*, while the time level at which the variables are unknown is *n+1*. From the values of the fluid dynamic quantities at the time $t^{(n)}$, by solving the structural motion equations, the structural displacements are calculated and, from the latter, the coordinates of the control volume vertices are updated and the grid velocity $u_{g,i}^{(n)}$ is calculated. Given the values of $\langle\overline{u}_i\rangle^{(n)}$, $\langle\overline{P}\rangle^{(n)}$, $\langle\overline{k}\rangle^{(n)}$, $\langle\overline{\omega}\rangle^{(n)}$ at the centre of the calculation cells at the time $t^{(n)}$, the calculation of the values of $\langle\overline{u}_i\rangle^{(n+1)}$, $\langle\overline{P}\rangle^{(n+1)}$, $\langle\overline{k}\rangle^{(n+1)}$, $\langle\overline{\omega}\rangle^{(n+1)}$ at the time $t^{(n+1)}$ is performed by integrating the fluid motion equations (supplied with the turbulence closure relations for the Reynolds stress tensor).

In the solution procedure for the fluid motion equations, a five stage fourth order accurate Strong Stability Preserving Runge-Kutta (SSPRK) fractional-step method is used for the momentum equations and a pressure correction formulation is applied to obtain a divergence free velocity field at each time level. Having indicated with $\langle\overline{u}_i\rangle^{(n)}$ the value of the *i-th* component of the fluid velocity field at the time level *n*, the following five stage iteration procedure is adopted in order to calculate the fluid velocity field $\langle\overline{u}_i\rangle^{(n+1)}$ at the time level *n+1*. Let be

$$\langle\bar{u}_i\rangle^{(0)} = \langle\bar{u}_i\rangle^{(n)} \quad (7).$$

At each stage *p* (where *p = 1,2,... 5*), an intermediate velocity field $\langle\overline{u}_i\rangle^{*(p)}$ is obtained explicitly through Eq. (2) by using the values of the previous time level

$$\langle\bar{u}_i\rangle^{*(p)} = \sum_{q=0}^{p-1}\left[\Omega_{pq}\langle\bar{u}_i\rangle^{(q)} + \Delta t\,\varphi_{pq}\,D\left[\langle u_i\rangle^{(q)}, t^{(n)} + d_q\Delta t\right]\right] \quad (8)$$

being $D(\langle u_i\rangle,t)$ equal to the right-hand side of Eq. (2) divided for ΔA, in which the pressure gradient term has been ignored. For the values of the coefficients Ω_{pq}, φ_{pq} and d_q refer to Spiteri and Ruuth [29]. In general, the requirement to satisfy the continuity

equation is not met by the intermediate velocity field of Eq. (8). Therefore, the velocity and the pressure field are corrected as follows. By introducing a scalar potential ψ, the well known Poisson pressure equation in integral form reads:

$$\int_L \frac{\partial \psi^{(p)}}{\partial x_i}\, n_i\, dL = -\int_L \langle \bar{u}_i \rangle^{*(p)}\, n_i\, dL \qquad (9)$$

where L and n_i are respectively the contour of the calculation cell and the *i-th* component of the unit outward vector normal to the contour. The calculation of the above scalar potential ψ is performed by solving Eq. (9). The corrector velocity field $\langle \bar{u}_i \rangle^c$ is calculated by means of the relation

$$\langle \bar{u}_i \rangle^{c(p)} = \frac{\partial \psi^{(p)}}{\partial x_i} \qquad (10).$$

The velocity field $\langle \bar{u}_i \rangle^p$ at the stage p is given by

$$\langle \bar{u}_i \rangle^{(p)} = \langle \bar{u}_i \rangle^{*(p)} + \langle \bar{u}_i \rangle^{c(p)} \qquad (11).$$

The velocity and pressure fields at the time $t^{(n+1)}$ are respectively given by

$$\langle \bar{u}_i \rangle^{(n+1)} = \langle \bar{u}_i \rangle^{(5)}, \quad \langle \bar{P} \rangle^{(n+1)} = \frac{1}{\Delta t}\psi^{(5)} \qquad (12).$$

The calculation of the term $D(\langle u_j \rangle, t)$ require the numerical approximations of the integrals on the right-hand side of Eq. (2). This calculation is based on the following passages:

1. High order WENO reconstructions, from cell averaged values, of the point values of the unknown variables at the centre of the contour segments which define the calculation cells. At the centre of the contour segment which is common with two adjacent cells, two point values of the unknown variables are reconstructed by means of two WENO reconstructions defined on two adjacent cells.
2. Advancing in time of the point values of the unknown variables at the centre of the contour segments by means of the so-called exact solution of the Riemann problem, with initial data given by the pair of point values computed by two WENO reconstructions defined on the two adjacent cells.
3. Calculation of the spatial integrals which define $D(\langle u_j \rangle, t)$.

Further details regarding the WENO reconstructions, the advancing in time of the unknown variables and the calculation of the spatial integrals which define $D(\langle u_j \rangle, t)$ can be found in Gallerano and Cannata [30], Gallerano et al. [31] and Gallerano et al. [32]. The numerical integration of the turbulence closure relations makes it possible to calculate $\langle \bar{k} \rangle^{(n+1)}$, $\langle \bar{\omega} \rangle^{(n+1)}$ and the Reynolds stress tensor at the time $t^{(n+1)}$ through Eq. (3). The discretisation of Eqs. (8) and (9) by means of the numerical method introduced above entails the risk of introducing mass sources or sinks in the flow field, if the grid velocity $u_{g,i}$ and the change of volume over time are not treated consistently. For this reason, the Geometric Conservation Law (GCL)

$$\frac{d}{dt}\int_{\Delta A} dA + \int_{\Delta A} \frac{\partial u_{g,i}}{\partial x_i}\, dA = 0 \qquad (13)$$

has to be satisfied. In order to warrant consistency, Eq. (13) is used to determine the grid velocity by the given change of volume of the computational cell [26]. In order to update the coordinates of the control volume vertices at all times, a mesh movement algorithm based on using Inverse Distance Weighting [33] is used in order to interpolate the displacements of the boundary nodes to the whole flow mesh.

3 Results and discussion

In this section, the proposed simulation model is utilised to analyse the full fluid-structure interaction of the Forth Road Bridge deck. Table 1 lists the full-scale geometric and structural properties used in the fluid-structure interaction analysis, which are taken from Robertson et al. [9].

Table1: full-scale properties of the Forth Road Bridge deck

Overall width	31.2 *m*
Maximum depth	3.2 *m*
Unit length mass	17.3 x 10^3 *kg/m*
Unit length moment of inertia	2.13 x 10^6 *kgm²/m*
Heaving natural frequency	0.174 *Hz*
Torsional natural frequency	0.4 *Hz*
Heaving damping ratio	0.31%
Torsional damping ratio	0.14%

3.1 Geometry and numerical modelling

The results shown later (see the following subsections) are obtained by using a block-

structured grid which is made up of 272464 cells. In this grid, a geometric progression of 1.02 for the cell size varying is used in all directions. The dimensions of the computational domain in the x and y directions are respectively equal to $Dx = 10B$ e $Dy = 5B$ (being B the width of the cross-section of the deck). In each simulation, the adopted Reynolds number correspond to that derived from the full-scale wind velocity U, the air kinematic viscosity ν (which is equal to 1.23×10^{-5} m^2/s) and the cross-section width B. The time step is derived by imposing the Courant number to be less than 0.9 in all the simulations: e.g., for the simulation performed at $Re = 1.95 \times 10^8$ (U = 87.4 m/s) this prescription produces a minimum time step close to $\Delta t = 1 \times 10^{-5}$ s.

For the fluid pressure, a zero gradient boundary condition is applied at the inflow of the domain, while at the domain outlet a constant pressure boundary condition is applied. For the other quantities (fluid velocity, turbulent kinetic energy and turbulence frequency) a constant value is imposed at the inflow, while a zero gradient boundary condition is applied for the same quantities at the outlet. The near-wall treatment proposed by Menter et al. [34], which permits to switch automatically from a classical low-Re formulation on fine grids to a wall function formulation on coarser meshes, is used at the solid walls.

3.2 Model validation

The model validation is performed by comparing the numerical results with those obtained from the wind tunnel tests described in the work of Robertson et al. [9].

Fig. 1 shows the plot of the damping coefficient of the rotations against the reduced velocity U_θ of the wind ($U_\theta = U / (f_\theta B) = 6.34$, being f_θ the natural torsional frequency of the deck). From Fig. 1 it can observed that the reduced critical velocity obtained by the proposed model is $U_\theta^* = 6.34$ (which corresponds to a full-scale critical wind velocity of 79.1 *m/s*). This value matches very well the experimental result of $U_\theta^* \approx 6.35$ reported by Robertson et al. [9].

Fig. 2 shows the plot of the root mean square of the rotations against the reduced velocity U_θ. In this figure, both the root mean square values obtained numerically in the present work and the experimental ones taken from Robertson et al. [9] are shown. By observing Fig. 2 it can be seen that the numerical results are in good agreement with the experimental ones.

Lastly, the frequencies of the rotational and the vertical motion of the deck are identified for the considered reduced velocities U_θ. In agreement with that reported by Robertson et al. [9], it is found that at the point of flutter instability the frequencies of the translational and rotational motion are identical. In particular, the synchronization frequency is found to be $f_\theta^* = 0.34$ *Hz*.

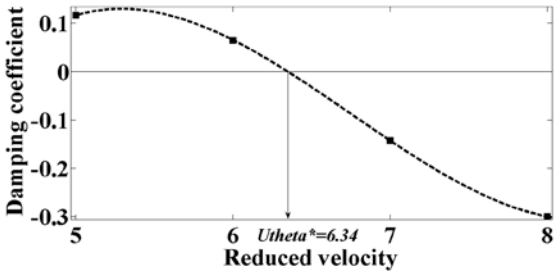

Fig. 1: Damping coefficients of the rotations against the reduced velocity

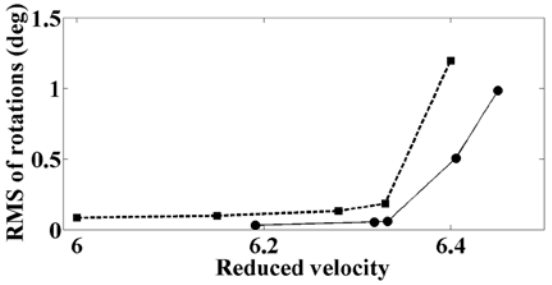

Fig. 2: Root-mean-square of the rotations against the reduced velocity

3.3 Flutter type characterization

According to Matsumoto et al. [5], the type of flutter affecting the Forth Road Bridge is characterised by means of the angle Ψ defined as the phase delay of the deck heaving response (vertical displacements) to the deck torsional response (rotations). These authors underline that the oscillatory motion of the cross-section of a bridge deck can be seen as the overlapping of two fundamental oscillatory motions. The first of these motions is named as *torsional fundamental mode* and mainly consists of a pure rotational motion around a certain point apart from the mid-chord point. In this first mode, the angle Ψ is equal to 0° (Fig. 3) or 180° (Fig. 4) depending on whether the centre of rotation is placed upstream or downstream the mid-chord point of the deck cross-section. The second of the above fundamental motions is named as *heaving fundamental mode* and consists of a prominent heaving motion with the accompany of

small torsional oscillations. In this second mode, the angle Ψ is equal to 90° (Fig. 5) or -90° (Fig. 6) depending on whether the sign of the small rotation of the upward moving cross-section is clockwise or anti-clockwise during the passage from the position of static equilibrium to a position of maximum relative height.

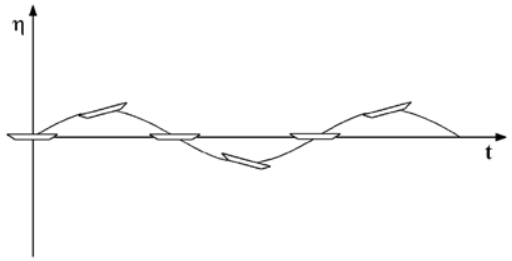

Fig. 3: Torsional fundamental mode, $\Psi = 0°$

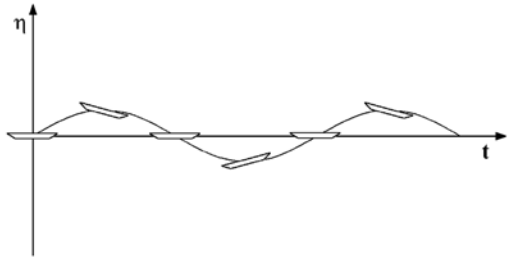

Fig. 4: Torsional fundamental mode, $\Psi = 180°$

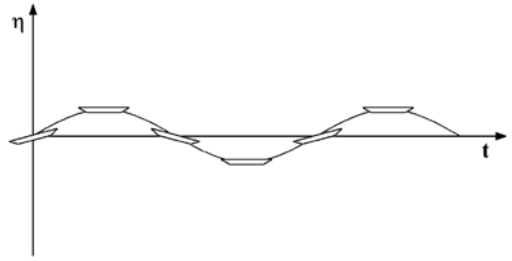

Fig. 5: Heaving fundamental mode, $\Psi = 90°$

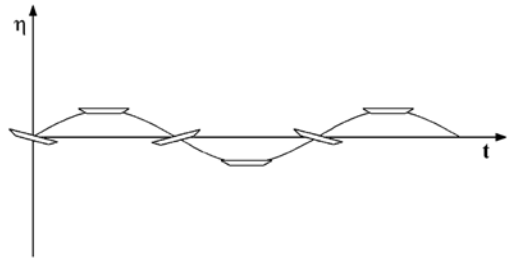

Fig. 6: Heaving fundamental mode, $\Psi = -90°$

Having introduced the flutter fundamental modes, the above authors distinguish a torsional-branch (TB) coupled flutter and a heaving-branch (HB) coupled flutter. In particular, the coupled flutter is of TB type if the torsional fundamental mode dominates on the heaving fundamental mode. In the case under examination (Forth Road Bridge), the angle Ψ is found to be equal to -16°, so that the relative contribution of the torsional and the heaving fundamental mode can be respectively quantified as $|cos\ (-16°)| = 0.96$ and $|sen\ (-16°)| = 0.27$. It is thus concluded that the Forth Road Bridge deck is prone to a TB coupled flutter in which the torsional fundamental mode clearly dominates the heaving fundamental mode.

3.4 Coupled flutter onset mechanism

Below the onset mechanism of coupled flutter is shown. For this purpose, the evolution of the aerodynamic forces and the structural displacements produced for a wind speed $U = 87.4$ *m/s* ($U_\theta = 7.0$) is investigated during a cycle of structural oscillations in which the amplitudes of vibration are still limited. Fig. 7 shows together the time history of the resultant of the unit-area forces exerted by the fluid on the deck surface and the time history of the infinitesimal vertical displacement of the centre of gravity of the deck. Fig. 8 shows together the time history of the twisting moment produced by the above resultant force and the time history of the infinitesimal deck rotation. The structural oscillation cycle shown in Figs. 7, 8 is delimited by two time instants (indicated as A and E) at which a relative minimum value is assumed by the infinitesimal vertical displacement of the downward moving gravity centre of the structure. By observing Fig. 7 it can be deduced that, in the time intervals A-B and D-E of the considered cycle, the force resultant acts against the vertical motion of the centre of gravity whereas, during the time interval B-D, the same resultant acts in favour of the translational motion. The integral of the work performed by the force resultant over the infinitesimal displacement of the centre of gravity during the time interval B-D is around equal to 260 *kJ*. This value is found to be considerably higher, in modulus, than the value obtained by adding the integral of the work performed during the time interval A-B (around -100 *kJ*) and the integral of the work performed during the time interval D-E (around -60 *kJ*). It follows that the net input of energy (roughly 100 *kJ*) of the aerodynamic resultant force to the translational motion is to destabilise the motion itself. Similar considerations apply to the effect of

the twisting moment produced by the above resultant force to the rotational motion. Fig. 8 shows that, in the time intervals A-B1 and D1-E, the above moment acts in favour of the rotational motion of the deck, thus providing an amplification effect of the motion itself. By contrast, during the time interval B1-D1, the twisting moment acts against the rotational motion and, consequently, produces a damping effect of the motion itself. The integral of the work performed by the twisting moment over the infinitesimal deck rotation during the entire cycle A-E is around equal to 25 *kJ*. It can be deduced that the net input of energy of the aerodynamic twisting moment to the rotational motion is to destabilise the motion itself.

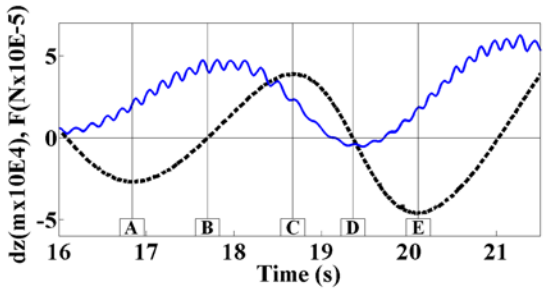

Fig. 7: Time histories of the resultant of the unit-area forces exerted by the fluid on the deck surface (blue) and of the infinitesimal vertical displacement of the centre of gravity of the deck (black, dashed)

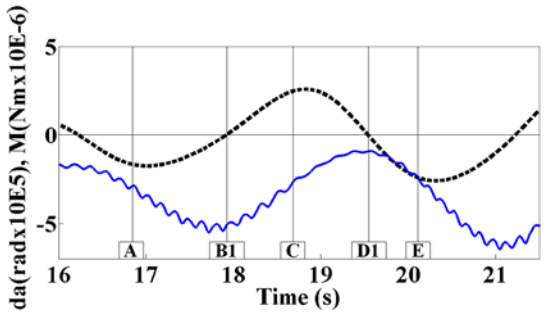

Fig. 8: Time histories of the resultant of the aerodynamic twisting moment (blue) and of the deck rotation (black, dashed)

On the basis of the above consideration, it is possible to conclude that the reason for the onset of the instability resides in the fact that there are some temporal fractions, within each of the first oscillation cycles, in which the aerodynamic field provides both the translational and the rotational motion with a higher supply of energy than that subtracted from the deck motion in the rest of the cycle.

After the instability of the roto-translational motion has been triggered, the maximum amplitude of the rotation angle progressively increases. As shown in the following subsection, once the above angle exceeds a threshold value the leading edge recirculation bubble, which pulsates in the onset phase just described, starts to drift along the deck surface. From this point on, the modalities by which the oscillations amplify are different to those described before in the present subsection.

3.5 Post-critical flutter mechanism

Below the amplification mechanism of coupled flutter is shown. For this purpose, the evolution of the aerodynamic fields and the structural motion developed for a wind speed $U = 87.4$ *m/s* ($U_\theta = 7.0$) is investigated during a cycle of structural oscillations in which the deck exhibits large amplitudes of vibration. Figs. 9-12 show the fluid velocity field which form around the deck in four time instants T1-T4 included in ½ of the above cycle. It is intended by ½ cycle the time interval delimited by the instant when the gravity centre of the downward moving structure corresponds to the static equilibrium position of the structure's centre of gravity and the instant when the gravity centre of the upward moving structure corresponds to the static equilibrium position of the structure's centre of gravity. Figs. 13-16 show the distribution of the surface normal unit-area forces exerted by the fluid on the deck (aerodynamic forces) in the same time instants.

By examining Figs. 9-12 and Figs. 13-16 it can be deduced that the instability amplification is due to the formation and drift of large-scale vortices on the surface of the deck. From the simulation it is possible to deduce that the resultant of the surface normal unit-area forces exerted by the fluid on the deck surface moves with the vortical formation generated at the leading edge. The point of application of this resultant is placed at the vortical formation. Therefore, the movement of this resultant with respect to the shear centre gives rise to a twisting moment which varies in intensity and direction during the deck oscillation. In particular, the sign of this twisting moment is found to be always coherent with the sign of the instantaneous angular velocity. Consequently, there is a continuous supply of energy from the fluid dynamic field to the structure, that constitutes the reason for the amplification of the instability of the torsional motion. The integral of the work performed by the resultant of the aerodynamic forces over the infinitesimal displacement of the centre of gravity

during the entire cycle is positive. Consequently, the net effect of the resultant on the translational motion of the deck is to amplify the above-mentioned motion and provide a destabilising contribution.

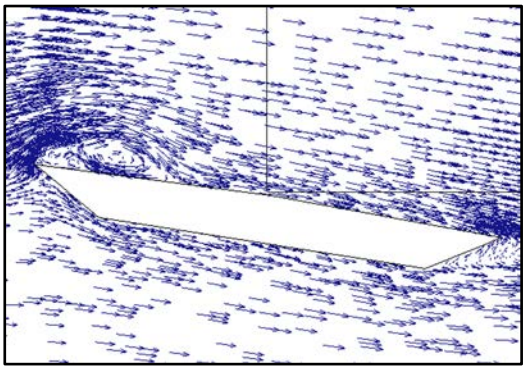

Fig. 9: Fluid velocity field around the deck at T1

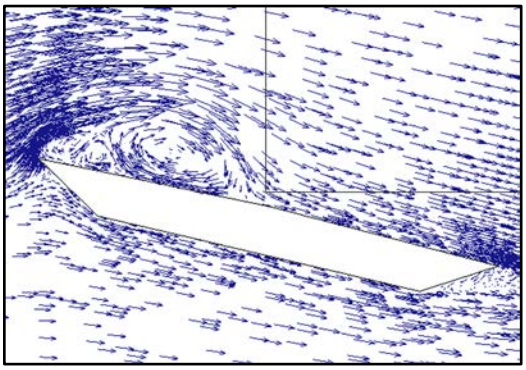

Fig. 10: Fluid velocity field around the deck at T2

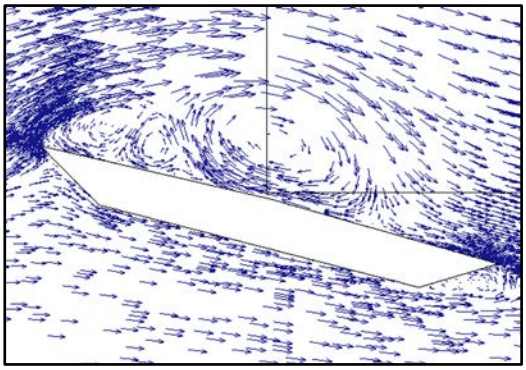

Fig. 11: Fluid velocity field around the deck at T3

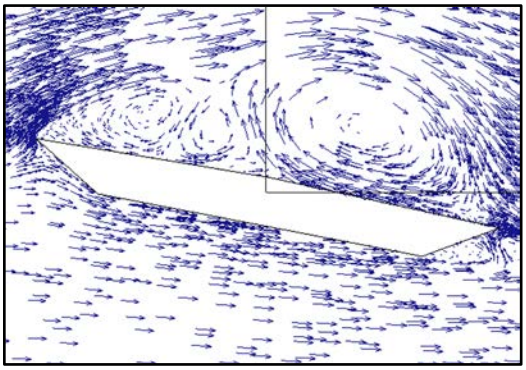

Fig. 12: Fluid velocity field around the deck at T4

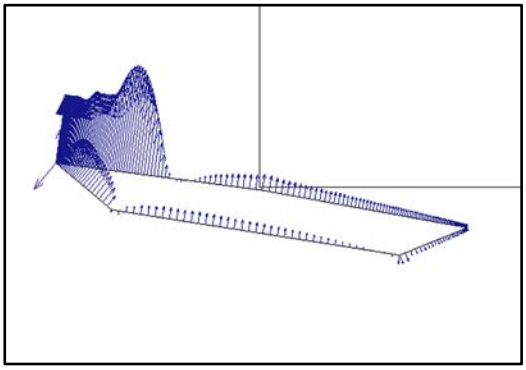

Fig. 13: Distribution of the unit-area fluid forces at T1

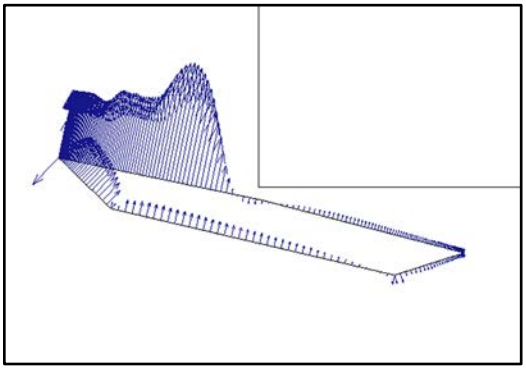

Fig. 14: Distribution of the unit-area fluid forces at T2

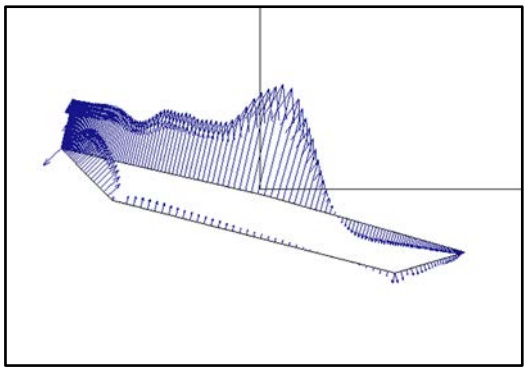

Fig. 15: Distribution of the unit-area fluid forces at T3

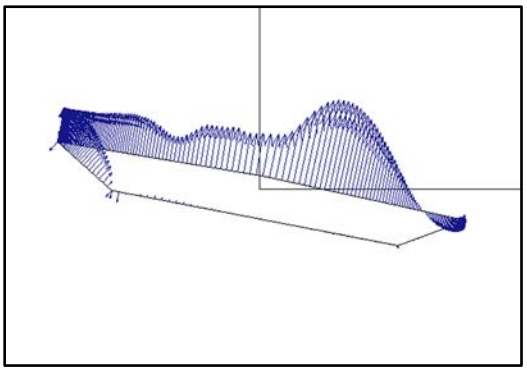

Fig. 16: Distribution of the unit-area fluid forces at T4

4 Conclusions

In this work the aeroelastic stability of long-span bridge decks has been numerically investigated. A simulation model has been presented by which the aerodynamic fields and the structural motion are simultaneously and jointly simulated. The validation of the numerical model has been performed by comparing the numerical results with those of an experimental campaign, in terms of critical wind flutter velocity and root-mean-square of the deck rotational displacements, and has been used to investigate the aeroelastic stability of the Forth Road Bridge deck.

A profound insight into the onset and the amplification mechanisms of coupled flutter for long-span bridge decks is proposed. It has been demonstrated that the reason for the onset of the instability resides in the fact that there are some temporal fractions, within each of the first oscillation cycles, in which the aerodynamic field provides both the translational and the rotational motion of the deck with a higher supply of energy than that subtracted from the motion itself in the rest of the cycle. Once the instability has been triggered, the amplitudes of vibrations increase at each cycle until the leading edge recirculation bubble, which pulsates for small oscillation amplitudes, bursts producing large vortical formations which drift along the upper side of the bridge deck. The drifting of this vortical formations has been found to be the reason for the amplification of the instability. It has been shown that the sign of the twisting moment produced by the aerodynamic field on the structure is always coherent with that of the rotation. Consequently, there is a continuous supply of energy from the fluid dynamic field to the structure, that constitutes the key to the amplification of the instability of the torsional motion.

References:

[1] E. Dowell, *A Modern Course in Aeroelasticity: Fifth Revised and Enlarged Edition*, Springer, 2014.

[2] A. Larsen, Aerodynamics of the Tacoma Narrows Bridge – 60 Years Later, *Structural Engineering International*, Vol.10, No.4, 2000, pp. 243-248.

[3] F. L. Haan, *The effects of turbulence on the aerodynamics of long-span bridges*, PhD Thesis, University of Notre Dame, 2000.

[4] J. B. Frandsen, Numerical bridge deck studies using finite elements. Part I: flutter, *Journal of Fluids and Structures*, Vol.19, No.2, 2004, pp. 171–191.

[5] M. Matsumoto, H. Matsumiya, S. Fujiwara, Y. Ito, New consideration on flutter properties based on step-by-step analysis, *Journal of Wind Engineering and Industrial Aerodynamics*, Vol.98, No.12, 2010, pp. 429-437.

[6] R. H. Scanlan, J. J. Tomko, Airfoil and bridge deck flutter derivatives, *Journal of the Engineering Mechanics Division-ASCE*, Vol.97, 1971, pp. 1717–1737.

[7] M. A. Astiz, Flutter stability of Very Long Suspension Bridges, *Journal of Bridge Engineering*, Vol.3, No.3, 1998, pp. 132-139.

[8] R. P. Selvam, S. Govindaswamy, H. Bosch, Aeroelastic analysis of bridges using FEM and moving grids, *Wind and Structures*, Vol.5, No.2_3_4, 2002, pp. 257-266.

[9] I. Robertson, S. J. Sherwin, P. W. Bearman, Flutter instability prediction techniques for bridge deck sections, *International Journal for Numerical Methods in Fluids*, Vol.43, No.10-11, 2003, pp. 1239-1256.

[10] A. L. Braun, A. M. Awruch, Finite element simulation of the wind action over bridge sectional models: Application to the Guamà River Bridge (Parà State, Brazil), *Finite Elements in Analysis and Design*, Vol.44, No.3, 2008, pp. 105-122.

[11] S. Oka, T. Ishihara, Numerical study of aerodynamic characteristics of a square prism in a uniform flow, *Journal of Wind Engineering and Industrial Aerodynamics*, Vol.97, 2009, pp. 548-559.

[12] L. Bruno, S. Khris, The validity of 2D numerical simulations of vortical structures around a bridge deck, *Mathematical and Computer Modelling*, Vol.37, No.7-8, 2003, pp. 795–828.

[13] F. Cioffi, F. Gallerano, From rooted to floating vegetal species in lagoons as a consequence of the increases of external nutrient load: An analysis by model of the species selection mechanism, *Applied Mathematical Modelling*, Vol.30, No.1, 2006, pp. 10-37.

[14] Y. Cheng, F. S. Lien, E. Yee, R. Sinclair, A comparison of Large Eddy Simulations with a standard k–ε Reynolds-averaged Navier–Stokes model for the prediction of a fully developed turbulent flow over a matrix of cubes, *Journal of Wind Engineering and Industrial Aerodynamics*, Vol.91, 2003, pp. 1301-1328.

[15] F. Gallerano, G. Cannata, Compatibility between reservoir sediment flushing and river protection, *Journal of Hydraulic Engineering*, Vol.137, No.10, 2011, pp. 1111-1125.

[16] Md. N. Haque, H. Katsuchi, H. Yamada, M. Nishio, Flow field analysis of a pentagonal-shaped bridge deck by unsteady RANS, *Engineering Applications of Computational Fluid Mechanics*, Vol.10, No.1, 2015, pp. 1-16.

[17] F. Gallerano, G. Cannata, F. Lasaponara, A new numerical model for simulations of wave transformation, breaking and long-shore currents in complex coastal regions, *International Journal for Numerical Methods in Fluids*, Vol.80, 2015, pp. 571-613.

[18] F. Gallerano, G. Cannata, F. Lasaponara, Numerical simulation of wave transformation, breaking and runup by a contravariant fully non-linear Boussinesq equations model, *Journal of Hydrodynamics (Ser. B)*, Vol.28, No.3, 2016, pp. 379-388.

[19] Z. Zhu, M. Gu, Z. Chen, Wind tunnel and CFD study on identification of flutter derivatives of a long-span self-anchored suspension bridge, *Computer-Aided Civil and Infrastructure Engineering*, Vol.22, No.8, 2007, pp. 514–554.

[20] S. De Miranda, L. Patruno, F. Ubertini, G. Vairo, On the identification of flutter derivatives of bridge decks via RANS turbulence models: Benchmarking on rectangular prisms, *Engineering Structures*, Vol.76, 2014, pp. 359-370.

[21] F. Nieto, D. M. Hargreaves, J. S. Owen, S. Hernandez, On the applicability of 2D URANS and SST k-ω turbulence model to the fluid-structure interaction of rectangular cylinders, *Engineering Applications of Computational Fluid Mechanics*, Vol.9, No.1, 2015, 157-173.

[22] M.W. Sarwar, T. Ishihara, Numerical study on suppression of vortex-induced vibrations of box girder bridge section by aerodynamic countermeasures, *Journal of Wind Engineering and Industrial Aerodynamics*, Vol.98, 2010, pp. 701-711.

[23] C. Mannini, A. M. Marra, G. Bartoli, VIV–galloping instability of rectangular cylinders: review and new experiments, *Journal of Wind Engineering and Industrial Aerodynamics*, Vol.132, 2014, pp. 109-124.

[24] C. Mannini, A. Soda, G. Schewe, Unsteady RANS modelling of flow past a rectangular cylinder: Investigation of Reynolds number effects, *Computers & Fluids*, Vol.39, 2010, pp. 1609-1624.

[25] K. Shimada, T. Ishihara, Predictability of unsteady two-dimensional k-ε model on the aerodynamic instabilities of some rectangular prisms, *Journal of Fluids and Structures*, Vol.28, 2011, pp. 20–39. C. Hertel, M. Schumichen, S. Lobig, J. Frohlich, J. Lang, Adaptive large eddy simulation with moving grids, *Theoretical and Computational Fluid Dynamics*, Vol.27, 2013, pp. 817-841.

[27] F. R. Menter, Review of the shear-stress transport turbulence model experience from an industrial perspective, *International Journal of Computational Fluid Dynamics*, Vol.23, No.4, 2009, pp. 305-316.

[28] L. Li, S. J. Sherwin, P. W. Bearman, A moving frame of reference algorithm for fluid/structure interaction of rotating and translating bodies, *International Journal for Numerical Methods in Fluids*, Vol.38, No.2, 2002, pp. 187-206.

[29] R. J. Spiteri, S. J. Ruuth, A new class of optimal high-order strong-stability preserving time discretization methods, *SIAM Journal on Numerical Analysis*, Vol.40, No.2, 2002, pp. 469-91.

[30] F. Gallerano, G. Cannata, Central WENO scheme for the integral form of contravariant shallow-water equations, *International Journal for Numerical Methods in Fluids*, Vol.67, No.8, 2011, pp. 939-959.

[31] F. Gallerano, G. Cannata, M. Tamburrino, Upwind WENO scheme for Shallow Water Equations in contravariant formulation. *Computer & Fluids*, Vol.62, 2012, pp. 1-12.

[32] F. Gallerano, G. Cannata, M. Villani, An integral contravariant formulation of the fully non-linear Boussinesq equations, *Coastal Engineering*, Vol.83, 2014, pp. 119-136.

[33] L. Uyttersprot, *Inverse Distance Weighting Mesh Deformation*, Master of Science Thesis, Delft University of Technology, 2014.

[34] F. Menter, J. Carregal Ferreira, T. Esch, B. Konno, The SST Turbulence Model with Improved Wall Treatment for Heat Transfer Predictions in Gas turbines, *Proceedings of the International Gas Turbine Congress*, Tokyo, Japan, 2003.